NUMERICAL SIMULATION OF SUPERCRITICAL SHOCK WAVE IN CHANNEL CONTRACTION

MING-HSI HSU[1]†, WEI-HSIEN TENG[2] and CHINTU LAI[3]

Department of Agricultural Engineering/Hydraulic Research Laboratory, National Taiwan University.
Taipei, Taiwan R.O.C.
[2]Department of Agricultural Engineering, National Taiwan University, Taipei, Taiwan R.O.C.
[3]Hydraulic Research Laboratory, National Taiwan University, Taipei, Taiwan R.O.C.

Abstract—The shock wave is a discontinuous profile of rapidly varied flow. A series of shock waves in channel contraction are numerically simulated and their results are verified using experimental data. Based on time- and space-marching approaches, two high-resolution finite-difference numerical schemes are applied for simulation of two-dimensional oblique shock waves. To initiate the simulation, the body-fitted coordinate transformation is employed to fit the channel boundary geometry, which is then followed by a set of well designed and controlled numerical simulations. The experimental data of Ippen and TPWCB are used to examine the validity of numerical results. © 1998 Elsevier Science Ltd. All rights reserved

1. INTRODUCTION

Supercritical flow through a channel contraction that results in oblique shock waves can be described by the two-dimensional shallow-water equation. With the assumptions of hydrostatic pressure distribution and mild channel-bed slope, the shallow water equation is reduced to the Saint-Venant type equations [1].

The Saint-Venant equations are a system of time-dependent nonlinear hyperbolic partial differential equations. Their solutions for supercritical flow in a channel contraction may contain discontinuity. It is not possible to analytically solve this nonlinear system of equations in their complete form. With the assumption of no energy loss by friction, Ippen [2] obtained analytical solutions for cases with small change in boundary angle. In most studies, researchers have resorted to numerical methods for their solutions. Various numerical methods have been proposed to address this class of problem. The non-oscillatory high-resolution finite-difference scheme based on Godunov's method has been developed for simulating aerodynamic problems with shock waves. Numerical models have also been formed to simulate the supercritical flow in channel contraction [4]. Garcia and Kahawita [3], and Fennema and Chaudhry [5], successfully introduced schemes of second order accuracy such as MacCormack, Lambda, Gugutti and Roe's TVD schemes to model the shock waves caused by dam break or channel contraction. By using shock-capturing techniques, Jimenez and Chaudhry [6], and Molls and Chaudhry [7] simulated a rapidly varied open channel flow from the depth averaged shallow-water equation.

The main purposes of this study are to develop and compare two approaches—time-marching and space-marching—that are considered useful for computation of supercritical shock waves, for their numerical behaviors and simulation effects, and to further look into model applicability with respect to the design characteristics of hydraulic structures.

In the following sections of this paper, the aim is first focused on the simulation of the two-dimensional supercritical flow in a channel contraction. Based on time-marching and space-marching approaches, two finite-difference schemes with an improved non-oscillatory shock-capturing method, i.e. time-marching and space-marching finite-difference schemes, are developed and used for simulation. The body-fitted coordinate transformation is employed to treat the

---

†Corresponding author.

boundary at the channel contraction. A series of numerical experiments have been conducted. The computed results are compared with the experimental data to demonstrate the validity of the numerical model.

2. GOVERNING EQUATIONS

Based on the assumptions that the pressure is hydrostatically distributed, that the unsteady flow in the channel is governed by the shallow-water principles in terms of mass and momentum conservations [8], that the channel has a rectangular cross-section, and that the channel bed varies smoothly, the two-dimensional shallow-water equation set can be derived in the conservation form:

$$U_t + F_x + G_y = S \tag{1}$$

The subscripts indicate partial differentiation. The above terms are defined as

$$U = [h, uh, vh]^T$$

$$F = [uh, u^2h + \frac{1}{2}gh^2, uvh]^T$$

$$G = [vh, uvh, v^2h + \frac{1}{2}gh^2]^T$$

$$S = [0, gh(S_{ox} - S_{fx}), gh(S_{oy} - S_{fy})]^T \tag{2}$$

in which, h represents the water depth; u and v, S_{ox} and S_{oy}, S_{fx} and S_{fy} correspond to the flow velocity components, bed slopes and the friction slopes along x- and y-axis, respectively. The friction slopes are expressed with Manning's formula as

$$S_{fx} = \frac{n^2 u\sqrt{(u^2 + v^2)}}{h^{4/3}}, \quad S_{fy} = \frac{n^2 v\sqrt{(u^2 + v^2)}}{h^{4/3}}$$

where n is the Manning roughness coefficient. The system of equations expressed in the form of Equation (1) is a hyperbolic type of partial differential equations. Equation (1) can also be written in the form [9] as follows

$$U_t + AU_x + BU_y = S \tag{3}$$

in which A and B are the Jacobian matrixes defined as

$$A = \frac{\partial F}{\partial U} = \begin{bmatrix} 0 & 1 & 0 \\ c^2 - u^2 & 2u & 0 \\ -uv & v & u \end{bmatrix} \quad B = \frac{\partial G}{\partial U} = \begin{bmatrix} 0 & 0 & 1 \\ -uv & v & u \\ c^2 - v^2 & 0 & 2v \end{bmatrix} \tag{4}$$

where c is the celerity of gravity wave

$$c = \sqrt{gh}$$

The eigenvalues (Λ_x and Λ_y) and corresponding eigenvectors (Γ_x and Γ_y) of Equation (1) or Equation (3), can be derived as follows

$$\Lambda_x = [\lambda_x, \lambda_x^+, \lambda_x^-]^T = [u, u+c, u-c]^T, \quad \Gamma_x = \begin{bmatrix} 1 & 0 & 1 \\ u+c & 0 & u-c \\ v & 1 & v \end{bmatrix} \tag{5}$$

$$\Lambda_y = [\lambda_y, \lambda_y^+, \lambda_y^-]^T = [v, v+c, v-c]^T, \quad \Gamma_y = \begin{bmatrix} 1 & 0 & 1 \\ u & 1 & u \\ v+c & 0 & v-c \end{bmatrix} \tag{6}$$

Because the flow velocity exceeds the celerity of gravity wave in supercritical flow throughout the channel contraction, the solution may lead to spontaneous discontinuities with real physical

meaning. With most of the classical methods, it is not possible to simulate such discontinuities at the steep wave front of the water surface profile. In this study, the high-resolution finite-difference method is used to capture the wave front.

3. BODY-FITTED COORDINATE TRANSFORMATION

An approximation of the boundaries of a curvilinear physical system with the rectangular grids may introduce large errors [10]. The boundary fitted grids in irregular domain are used to solve the governing equations in transformed coordinates. The procedures of generating the curvilinear coordinate system are followed through the numerical solution of partial differential equations.

In a two-dimensional physical domain, the Cartesian coordinates x and y are used, whereas the coordinates in the computational domain are denoted by ξ and η. The general equations used for coordinate transformation are Poisson equations shown in the following [11]:

$$\xi_{xx} + \xi_{yy} = P(\xi, \eta)$$
$$\eta_{xx} + \eta_{yy} = Q(\xi, \eta) \tag{7}$$

where the source terms P and Q are specified functions of ξ and η, and are given by adjusting the coordinate system [12]. Equation (7) is transformed into the computational coordinates by interchanging the dependent and independent variables. The transformed equations are:

$$\alpha x_{\xi\xi} - 2\beta x_{\xi\eta} + \gamma x_{\eta\eta} + J^2(P x_\xi + Q x_\eta) = 0 \tag{8}$$

$$\alpha y_{\xi\xi} - 2\beta y_{\xi\eta} + \gamma y_{\eta\eta} + J^2(P y_\xi + Q y_\eta) = 0 \tag{9}$$

where,

$$\alpha = x_\eta^2 + y_\eta^2, \quad \beta = x_\xi x_\eta + y_\xi y_\eta, \quad \gamma = x_\xi^2 + y_\xi^2, \quad J = (x_\xi y_\eta - x_\eta y_\xi)^{-1}.$$

The physical coordinates, x and y, are determined by solving Equations (8) and (9) with the Dirichlet boundary conditions.

4. TIME-MARCHING APPROACH

Splitting method is used to discretize Equation (1) with the finite-difference operator L. The use of L operator on $U(x_i, y_j, t_n)$ yields:

$$U(x_i, y_j, t_{n+1}) = L_x^{\Delta t/2} \cdot L_y^{\Delta t} \cdot L_x^{\Delta t/2}(U(x_i, y_j, t_n)) \tag{10}$$

or in a compact form:

$$U_{i,j}^{n+1} = L_x^{\Delta t/2} \cdot L_y^{\Delta t} \cdot L_x^{\Delta t/2}(U_{i,j}^n) \tag{11}$$

In Equation (11), the scheme first advances a half-time step along the x-direction, then takes a full-time step on the y-direction, and finally another half-time step on the x-direction. This scheme has third-order accuracy in time as well as second-order accuracy in space [13]. When the L operator is performed in the y-direction, the variation in the x-direction is neglected, i.e. F_x is considered to be zero. Similarly, G_y is zero when L_x is processed. To illustrate the procedure $L_x^{\Delta t/2}$ is performed on $U_{i,j}^n$ from the discretized form of Equation (1) in a following manner,

$$L_x^{\Delta t/2}(U_{i,j}^n) = U_{i,j}^n - \frac{\Delta t}{2\Delta x_i}(\bar{F}_{i+1/2,j}^{n+1/4} - \bar{F}_{i-1/2,j}^{n+1/4}) + \frac{\Delta t}{2}\bar{S}_{i,j}^{n+1/4} \tag{12}$$

where, $\bar{F}_{i\pm1/2,j}^{n+1/4}$ and $\bar{S}_{i,j}^{n+1/4}$ are the time averaged flux and source/sink over $[t_n, t_{n+1/2}]$, respectively. Their exact values may be evaluated by integration over that time interval theoretically. Instead of the integration, the $\bar{U}^n$ is used to approximate the time averaged flux,

$$\bar{F}_{i+1/2,j}^{n+1/4} \approx F(\tilde{U}_{i,j}^n)$$

$$\bar{F}_{i-1/2,j}^{n+1/4} \approx F(\tilde{U}_{i-1,j}^n) \tag{13}$$

$\tilde{U}_{i,j}^n$, is obtained by Godunov's method [14], that is

$$\tilde{U}_{i,j}^n = U_{i,j}^n - \frac{\Delta t}{2\Delta x} \Gamma_{xi,j} \Lambda_{xi,j}^n \Gamma_{xi,j}^{-1} (U_{i+1,j}^n - U_{i-1,j}^n)$$

$$+ \frac{\Delta t}{2\Delta x^2} \Gamma_{xi,j} \mid \Lambda_{xi,j}^n \mid \Gamma_{xi,j}^{-1} (U_{i+1,j}^n - 2U_{1,j}^n + U_{i-1,j}^n) \tag{14}$$

where,

$$\mid \Lambda_{xi,j}^n \mid = \mathrm{diag}(\mid \lambda_{xi,j} \mid, \mid \lambda_{xi,j}^+ \mid, \mid \lambda_{xi,j}^- \mid)$$

in which, the symbols, $\Lambda_{xi,j}^n$ and $\Gamma_{xi,j}$, denote the eigenvalues and eigenvectors of Equation (1) at node (x_i, y_i) calculated from Equation (5). The function, diag($\cdot$), is a diagonal matrix function. The eigenvalues $\Lambda_{xi,j}^n$ are always positive for supercritical flow. The time averaged source/sink terms $\bar{S}_{i,j}^{n+1/4}$ over $[t_n, t_{n+1/2}]$ is approximated as

$$\bar{S}_{i,j}^{n+1/4} \approx S\left(\frac{\tilde{U}_{i,j}^n + \tilde{U}_{i-1,j}^n}{2}\right) \tag{15}$$

In order to capture the shock wave without oscillation for supercritical flow, $F(\tilde{U}_{i,j}^n)$ in Equation (13) should be expressed by a combination of an upwind flux $F_U(\tilde{U}_{i,j}^n)$ and a flux-limitation step [13], i.e.

$$F(\tilde{U}_{i,j}^n) = F_U(\tilde{U}_{i,j}^n) + \left[\frac{1}{2}\Lambda_{xi,j}^n(\mathrm{sgn}(v_i) - v_i)\Delta x_i \sigma_i^n\right] \tag{16}$$

where $v_i = 2\max(\lambda_{xi,j}, \lambda_{xi,j}^+, \lambda_{xi,j}^-)\Delta t/\Delta x_i$ and sgn($\cdot$) is a sign function that matrix elements equal to $+1$, -1, and 0 for positive, negative, and zero argument, respectively. In the above equation, the upwind flux, $F_U(\tilde{U}_{i,j}^n)$, is defined as

$$F_U(\tilde{U}_{i,j}^n) = F(U_{i,j}^n) + \Lambda_{xi,j}^p \alpha_{i,j} \Gamma_{xi,j} \tag{17}$$

in which, $\Lambda_{xi,j}^p = \min(\Lambda_{xi,j}^n, 0)$. The symbol, $\alpha_{i,j}$, is the coefficient of $\gamma_{xi,j}$ in an eigenvector expansion of $U_{i+1,j}^n - U_{i,j}^n$ [13], i.e.

$$\alpha_{i,j} = \frac{U_{j+1,j}^n - U_{i,j}^n}{\Gamma_{xi,j}} \tag{18}$$

The last term in Equation (16) is the flux-limiter for non-oscillation, in which σ_i^n is determined by the minmod slope function,

$$\sigma_i^n = \frac{1}{\Delta x_i} \mathrm{minmod}(U_{i+1,j}^n - U_{i,j}^n, U_{i,j}^n - U_{i-1,j}^n) \tag{19}$$

where the minmod function is defined as

$$\mathrm{minmod}(a, b) = \begin{cases} a, & \text{if } \mid a \mid < \mid b \mid, a \cdot b > 0 \\ b, & \text{if } \mid b \mid < \mid a \mid, a \cdot b > 0 \\ 0 & \text{if } \qquad a \cdot b \leq 0 \end{cases} \tag{20}$$

The minmod slope function used in σ_i^n of Equation (16) is to ensure non-oscillation. In other words, the total variation does not grow when $F(\tilde{U}_{i,j}^n)$ is calculated from Equation (16).

In a similar way, $L_y^{\Delta t}$ operator in Equation (11) is expressed as follows,

$$L_y^{\Delta t}(U_{i,j}^n) = U_{i,j}^n - \frac{\Delta t}{\Delta y_j}(\bar{G}_{i,j+1/2}^{n+1/2} - \bar{G}_{i,j-1/2}^{n+1/2}) + \Delta t \bar{S}_{i,j}^{n+1/2} \tag{21}$$

The numerical flux in y-direction, $G(\tilde{U}_{i,j}^n)$, is expressed in a similar way as Equation (16), recalling the definition $v_j = 2\max(\lambda_{yi,j}, \lambda_{yi,j}^+, \lambda_{yi,j}^-)\Delta t/\Delta y_j$.

$$G(\tilde{U}_{i,j}^n) = G_L(\tilde{U}_{i,j}^n) + [\frac{1}{2}\Lambda_{yi,j}(\text{sgn}(v_j) - v_j)\Delta y_j \sigma_j^n] \tag{22}$$

where

$$G_L(\tilde{U}_{i,j}^n) = G(\tilde{U}_{i,j}^n) + \Lambda_{yi,j}^p \alpha_{i,j}\Gamma_{yi,j} \tag{23}$$

$$\sigma_j^n := \frac{1}{\Delta y_j}\text{minmod}(U_{i,j+1}^n - U_{i,j}^n, U_{i,j}^n - U_{i,j-1}^n) \tag{24}$$

A set of appropriate values for the flow variables, u, v and h, at time zero are specified at all nodes. For a two dimensional–supercritical flow, inflow boundary conditions have to be treated as Dirichlet boundary conditions and specified at the upstream boundary.

Because the bottom shear stress in the governing equations is considered to account for all the flow resistance, the slip condition is taken as the boundary condition at the side walls. Hence, the resultant velocity at the solid wall surface is tangent to the wall. Chaudhry and Bhallamudi [10] investigated several wall boundary techniques for gas dynamics and hydrodynamics computations. They used the reflection procedure to set the slip condition. This procedure is adopted herein because it can account for the impact of the refraction angle of shock wave and wall reflection of the flow near the boundary. Figure 1 is a sketch of reflection procedure. With this procedure, the flow depth and the magnitude of the resultant velocity at the imaginary reflection point are assigned the same as those at the corresponding interior grid point, and the normal velocity at the wall is set to zero. If θ is the angle between the wall and the x-axis and α is the angle between the resultant velocity at the interior point and the x-axis, then the velocity components u and v at the reflection point are:

$$u = V\cos(2\theta - \alpha) \tag{25}$$

$$v = V\sin(2\theta - \alpha) \tag{26}$$

where V is the resultant velocity at the interior point. Equations (25) and (26) are valid for both channel contraction and expansion.

For time-marching schemes to be stable, the Courant-Friedrichs-Lewy (CFL) condition must be obeyed. The CFL condition for the two-dimensional flows is usually expressed as follows [15]:

$$C_r = \frac{(V + c)\Delta t}{\Delta x \Delta y}\sqrt{(\Delta x)^2 + (\Delta y)^2} \le 1 \tag{27}$$
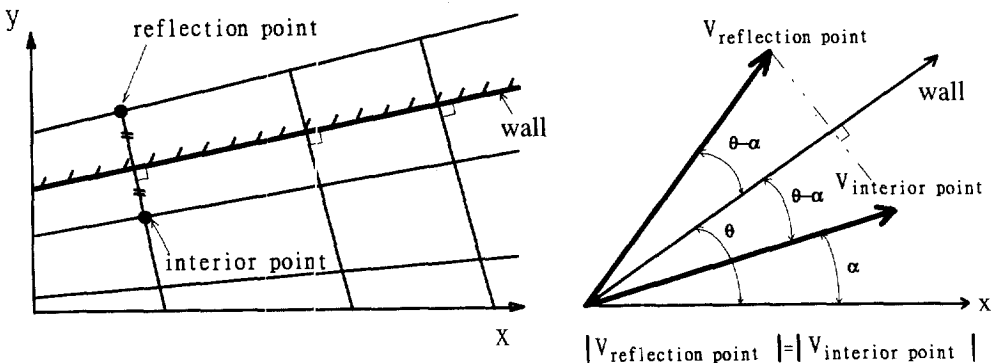
Fig. 1. Sketch of the reflection procedure for a wall [10].

5. SPACE-MARCHING APPROACH

For simulation of steady supercritical flow, the time derivative term of Equation (1) is dropped, i.e.

$$F_x + G_y = S \tag{28}$$

The Jacobin matrixes C and the eigenvalues Λ of Equation (28) can be derived as (shown in appendix)

$$C = \frac{\partial G}{\partial F} = \begin{bmatrix} \frac{uv}{u^2 - c^2} & \frac{-v}{u^2 - c^2} & \frac{u}{u^2 - c^2} \\ 0 & 0 & 1 \\ \frac{c^2(u^2 + v^2 - c^2)}{u(u^2 - c^2)} & \frac{-v^2}{(u^2 - c^2)} & \frac{v(2u^2 - c^2)}{u(u^2 - c^2)} \end{bmatrix} \tag{29}$$

$$\Lambda = [\lambda, \lambda^+, \lambda^-]^T = \left[\frac{v}{u}, \frac{uv + c^2\sqrt{Fr^2 - 1}}{u^2 - c^2}, \frac{uv - c^2\sqrt{Fr^2 - 1}}{u^2 - c^2} \right]^T \tag{30}$$

For a two-dimensional supercritical flow, the Froude numbers, $Fr = \sqrt{u^2 + v^2}/c$, are greater than 1.0 throughout the computational domain. The discretization of Equation (28) is made with respect to the space coordinates.

Finite-difference operator $L_x^{\Delta x}$ is used to discretize the first term of Equation (28),

$$F(x_{i+1}, y_j) = L_x^{\Delta x} F(x_i, y_j)$$

or

$$F_{i+1,j} = L_x^{\Delta x} F_{i,j} \tag{31}$$

where, $L_x^{\Delta x}$ is composed of backward-difference prediction step L_x^p, forward-difference correction step L_x^c, and flux-limitation step L_x^l, i.e.

$$L_x^{\Delta x} F_{i,j} = L_x^c L_x^p F_{i,j} - L_x^l F_{i,j} \tag{32}$$

These steps are elaborated as

(a) Backward-difference prediction step [16]

$$F_{i,j}^p = L_x^p F_{i,j} = F_{i,j} + \frac{\Delta x}{\Delta y}(G_{i,j} - G_{i,j-1}) + \Delta x S_{i,j} \tag{33}$$

The flow variables u, v and h at the prediction step are found by roots solver from the components of $F_{i,j}^p$, then $G_{i,j}^p$ and $S_{i,j}^p$, are calculated from Equation (2) using these flow variables.

(b) Forward-difference correction step [16]

$$F_{i,j}^c = L_x^c F_{i,j}^p = F_{i,j}^p - \frac{\Delta x}{\Delta y}(G_{i,j+1}^p - G_{i,j}^p) + \Delta x S_{i,j}^p \tag{34}$$

(c) Flux-limitation step [17]

$$L_x^l F_{i,j} = \left(1 - \frac{\phi(r_j) + \phi(1/r_j)}{2}\right) v(1 - v)(F_{i,j+1} - F_{i,j})$$

$$- \left(1 - \frac{\phi(r_{j-1}) + \phi(1/r_{j-1})}{2}\right) v(1 - v)(F_{i,j} - F_{i,j-1}) \tag{35}$$

where

$$r_j = (F_{i,j} - F_{i,j-1})/(F_{i,j+1} - F_{i,j})$$

$$\phi(r_j) = \begin{cases} \min(2r_j, 1); & r_j > 0 \\ 0; & r_j \leq 0 \end{cases}$$

$$v = \max(\lambda_{i,j}, \lambda_{i,j}^+, \lambda_{i,j}^-) \frac{\Delta x}{\Delta y}$$
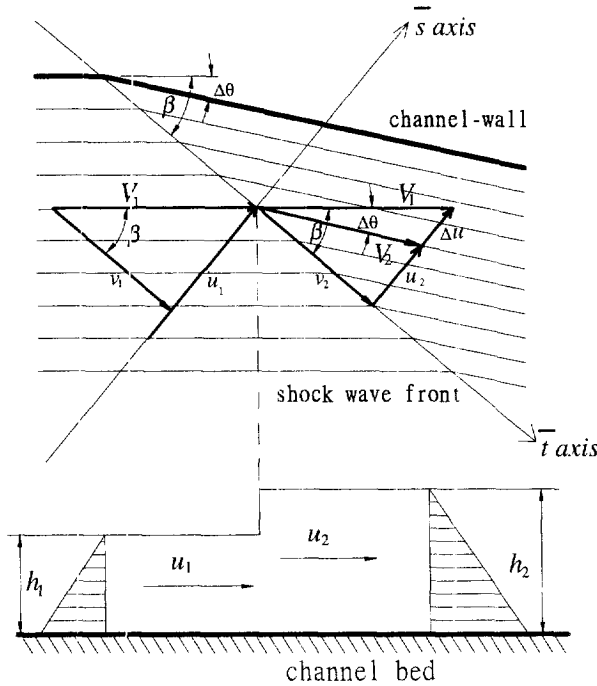
Fig. 2. Sketch of side-wall boundary conditions for space-marching approach.

To solve Equation (28), the Dirichlet boundary conditions are imposed on both the upstream boundary and the side walls. The upstream boundary conditions are given by specifying the water depth h and the velocity V. The side wall boundary conditions are derived from Equation (28), based on the assumption that the source/sink term is negligible along the wall, then Equation (28) becomes,

$$F_x + G_y = 0 \tag{36}$$

The physical curvilinear side wall can be approximated by numerical boundary grids with the technique of body-fitted coordinate transformation. The shock wave is caused by the deflection of a vertical channel-wall from each downstream grid to upstream grid through a finite angle $\Delta\theta$, as shown in Fig. 2. The refraction angle of the shock wave front is β. The exact solution for the shock-wave flow along the wall will be derived in the following manner. The vectors, $\bar{s}$ and $\bar{t}$ are defined as the directions of normal and tangent to the shock wave front. Equation (36) can be rewritten in the new coordinates as

$$F_s + G_t = 0 \tag{37}$$

or

$$\begin{bmatrix} \bar{u}h \\ \bar{u}^2 h + \frac{1}{2}gh^2 \\ \bar{u}\bar{v}h \end{bmatrix}_s + \begin{bmatrix} \bar{v}h \\ \bar{u}\bar{v}h \\ \bar{v}^2 h + \frac{1}{2}gh^2 \end{bmatrix}_t = 0 \tag{38}$$

where the $\bar{u}$ and $\bar{v}$ are the flow velocity components along the normal and tangent direction to the shock wave front, respectively. The derivatives of $\bar{u}$, $\bar{v}$ and h along the shock wave front can then be neglected.

$$h_t = 0, \quad \bar{u}_t = 0, \quad v_t = 0 \tag{39}$$

Hence, the term G_t in Equation (37) will be zero and Equation (37) is simplified as

$$(\bar{u}h)_{\bar{s}} = 0 \tag{40a}$$

$$(\bar{u}^2 h + \frac{1}{2}gh^2)_{\bar{s}} = 0 \tag{40b}$$

$$(\bar{u}\bar{v}h)_{\bar{s}} = 0 \tag{40c}$$

From Equation (40a), Equation (40c) can be rewritten as

$$\bar{v}_{\bar{s}} = 0 \tag{41}$$

Let subscripts 1 and 2 denote the upstream and downstream sides, respectively, of the shock wave front (shown in Fig. 2). Equations (40) and (41) can be expressed as follows,

$$h_1 \bar{u}_1 = h_2 \bar{u}_2 \tag{42a}$$

$$\bar{u}_1^2 h_1 + \frac{1}{2}gh_1^2 = \bar{u}_2^2 h_2 + \frac{1}{2}gh_2^2 \tag{42b}$$

$$\bar{v}_1 = \bar{v}_2 \tag{42c}$$

Since $\bar{u}_1 = V_1 \sin\beta$, combining Equation (42a) and (42b) yields,

$$h_2 = \frac{h_1}{2}(\sqrt{1 + 8F_1^2 \sin^2\beta} - 1) \tag{43}$$

in which, $Fr_1 = V_1/\sqrt{gh_1}$. The relationship among $\bar{u}_1$, $\bar{u}_2$, $\bar{v}_1$, $\bar{v}_2$, $\Delta\theta$ and β can be obtained from Fig. 2 that

$$\bar{v}_1 = \frac{\bar{u}_1}{\tan\beta}, \quad \bar{v}_2 = \frac{\bar{u}_2}{\tan(\beta - \Delta\theta)} \tag{44}$$

Because $\bar{v}_1 = \bar{v}_2$, the implicit functional form of β is [2]

$$\frac{\tan\beta(\sqrt{1 + 8Fr_1^2 \sin^2\beta} - 3)}{2\tan^2\beta - 1 + \sqrt{1 + 8Fr_1^2 \sin^2\beta}} = \tan\Delta\theta \tag{45}$$

The downstream velocity along the wall is obtained as follows

$$V_2 = V_1 \cos\beta \sec(\beta - \Delta\theta) \tag{46}$$

After the refraction angle of shock wave 'β' calculated from Equation (45) the given water depth h_1, the velocity V_1 and the wall-deflection angle $\Delta\theta$ along the side wall, the water depth h_2 and velocity V_2 can be determined from Equations (43) and (46), respectively. As a result of the velocity V_2 and the water depth h_2 calculated in process from upstream to downstream step by step, the side-wall boundary conditions are specified.

For the space-marching schemes to be stable, the symbol, v, which is defined in Equation (35) must satisfy the following condition.

$$v \leq 1 \tag{47}$$

6. SIMULATION RESULTS

6.1. Ippen's circular-arc channel contraction

A numerical simulation of the supercritical flow in a contracting channel designed and experimented by Ippen and Dawson [18] was performed. The channel has the Manning roughness coefficient of $n = 0.01$, and the upstream and downstream widths of 60.96 cm and 30.48 cm, respectively. They are each joined to the parallel walls at both ends by a horizontal circular-arc (see Fig. 3(a)). The water enters with flow depth of 0.254 cm (0.1 inch), velocity 70.9 cm/s, and
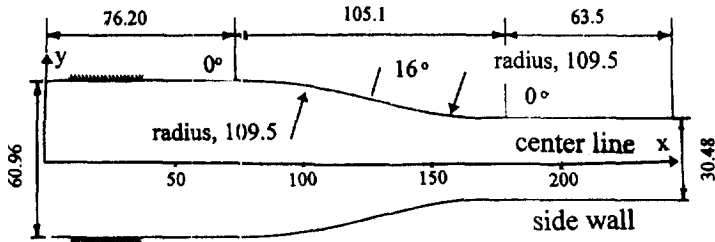
(a) Definition sketch for the channel contraction from Ippen's experiment (Ippen, 1951) (unit : centimeters)
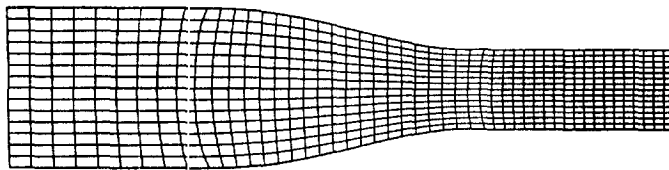

(b) boundary fitted grids (49x15) used for numerical simulation

Fig. 3. Definition sketch for the channel contraction and the boundary-fitted grids used for numerical simulation. (a) Definition sketch for the channel contraction from Ippen's experiment (Ippen, 1951). (b) Boundary fitted grids (49 × 15) used for numerical simulation.

the maximun stage along the center line
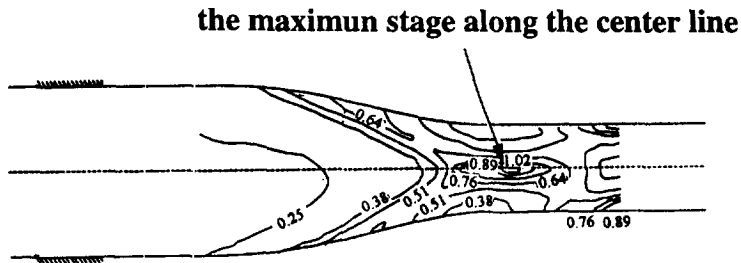
(a) measured (Ippen, 1951)
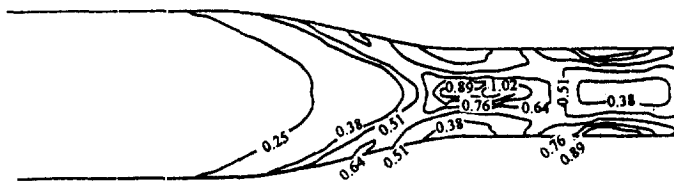
(b) simulated

Fig. 4. Measured and computed water depth contours for Ippen's circular-arc channel contraction. (a) Measured [2]. (b) Simulated.
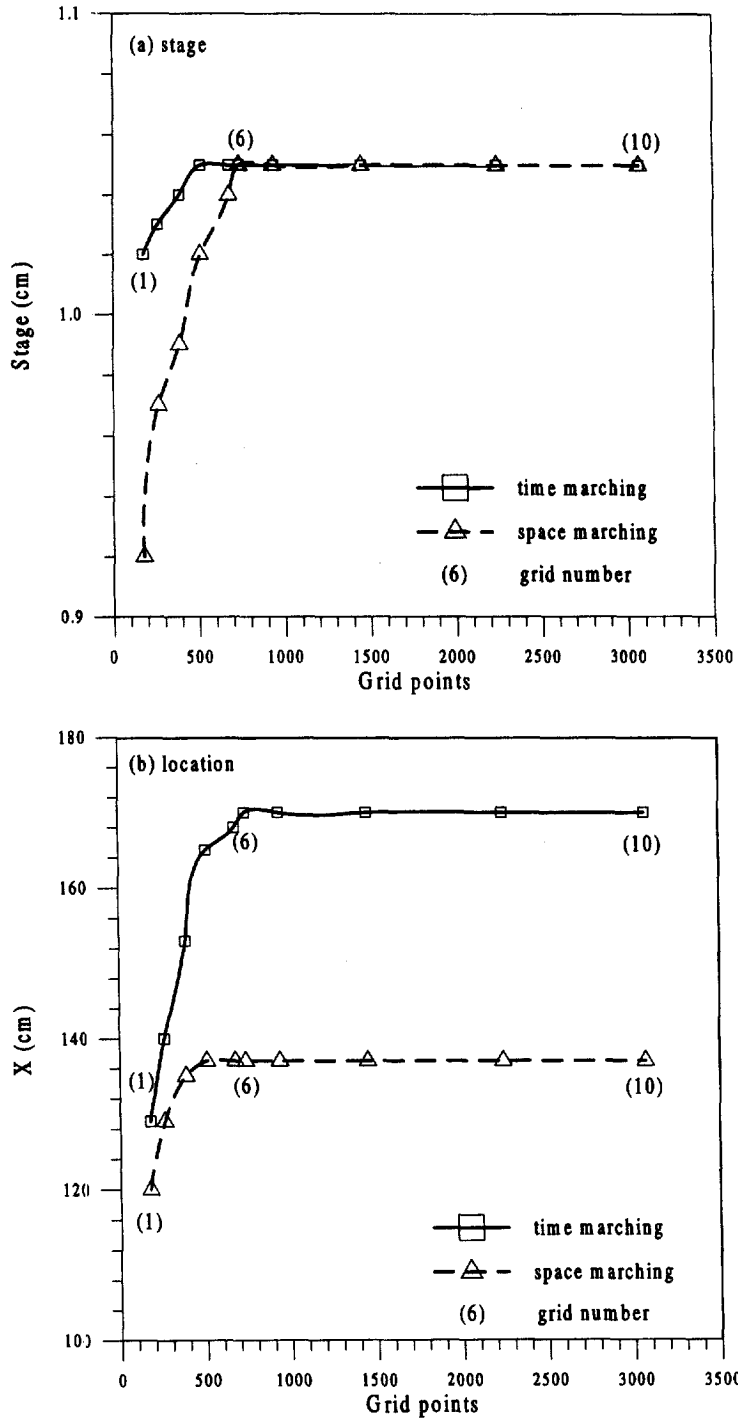
Fig. 5. The simulated maximum stage of standing shock wave and its location with various grid points.

the Froude number $Fr = 4.0$. Used in the numerical simulation is a boundary fitted grid of 49×15 (see Fig. 3(b)). The measured and simulated contours of flow depth, with time-marching scheme, are shown in Fig. 4(a) and (b). They are in good agreement with the experimental results given by Ipper and Dawson [18]. Figure 4(a) shows that the maximum stage along the center line of the channel is 1.04 cm caused by the standing shock wave. Figure 5(a) and (b) gives the comparison plots of the simulated maximum stage of the standing shock wave and its location with various grids. The simulated results achieve mesh-independence when the grid is

Table 1. The numerical experiment of mesh independence for Ippen's circular-arc channel contraction

Grid number	1	2	3	4	5	6	7	8	9	10
Grid	25 × 7	29 × 9	35 × 11	39 × 13	45 × 15	49 × 15	55 × 17	69 × 21	83 × 27	99 × 31
Grid points	175	261	385	507	675	735	935	1449	2241	3069
Relative error* (%)										
Time-marching	22.6	8.3	6.4	3.6	1.7	0.4	0.2	0.2	0.2	0.2
Space-marching	3.6	2.7	1.4	0.8	0.7	0.6	0.5	0.5	0.5	0.5
CPU time+ (min.)										
Time-marching	22.1	26.8	30.4	41.6	74.4	96.5	243.0	652.3	1469.2	3088.6
Space-marching	4.7	4.9	5.5	6.7	8.2	12.1	19.2	28.5	38.5	50.2

*Relative error = ABS(simulated stage – measured stage) ÷ measured stage × 100(%).
+The computer is Sun Spack 10 model 41

finer than 49×15. The comparison of the computer CPU time used and the relative error for different grids is shown in Table 1. It is obvious that the grid of 49×15 (grid number 6) is fine enough to produce accurate results within a reasonable computer CPU time. Figure 6(a) and (b) gives the comparison plots of two sets of computed profiles, one with time-marching and the other with space-marching, and one set of measured water-surface profiles, respectively, along the wall and the center line. There exist apparent phase differences among the results of the two numerical simulations and the experiment.

Figure 6 shows that the time-marching scheme gives better results than the space-marching scheme with respect to the phase of the shock waves. The different treatment of side-wall boundary conditions in the two schemes is the main reason for the differences in the simulated results. The time-marching scheme uses the reflected boundary techniques for the slip condition along the side-wall as stated earlier in this paper. In the space-marching scheme, based on an additional assumption that source/sink term is negligible along the wall, the side-wall boundary conditions including water depth and the velocity along the wall are calculated and specified as the Dirichlet boundary conditions for solving the flow field. However, there is no significant difference between the wave amplitudes from the two schemes as shown in Fig. 6. The space-marching scheme uses about one-eighth of the CPU time for the time-marching scheme when the grid of 49×15 (grid number 6) is used.

For lack of measured velocity data in this experiment, the Froude number and specific energy obtained from the numerical simulations are compared to each other in Fig. 7(a) and (b). The specific energy, E, is the total energy head above the channel bed and is defined as

$$E = h + \frac{V^2}{2g}$$

(48)

The results of the comparison show that the difference is manifest where the shock wave occurs. Further comparison of the experiments with the numerical results of both schemes will be made in the following section.

6.2. Experiments in TPWCB

In order to test the time- and space-marching numerical schemes, which are developed in this study, an experimental investigation was conducted at the Hydraulics Laboratory of Taiwan Provincial Water Conservancy Bureau (TPWCB). The experimental setup is a channel contraction composed of two converging straight walls in the upstream, with the angle 43.55° between them, and with two circular arcs at the transitions to the downstream parallel walls (Fig. 8). The roughness coefficient (n) is 0.01 and the bottom slope is 0.06. The discharge used in the experiments is 1.55×10^4 cm³/s. The upstream water depth is 1.0 cm and the velocity is 309.1 cm/s. The measured data, u, v and h, are specified for the upstream boundary condition at the left-end nodes.
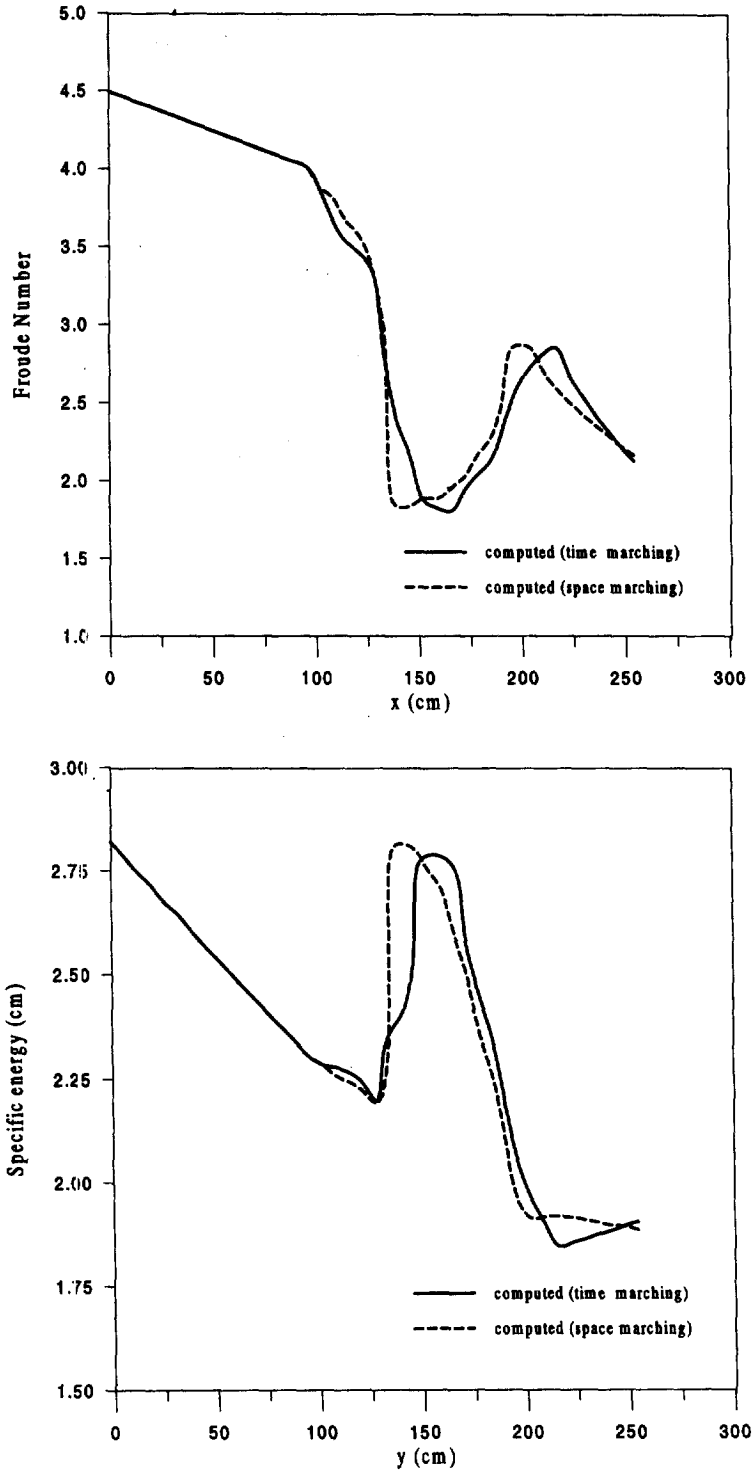
Fig. 6. Water surface profiles along the wall and the center line for Ippen's circular-arc channel contraction.

A boundary fitted grid of 52 × 15 was used in the numerical simulation. The simulated results are shown in Figs 9, 10, 11 and 12. The computed results are in good agreement with the measured data. Figure 9(a) and (b) show the comparison of the computed and measured water-surface profiles along the wall and the center line, respectively. They show that the time-march-
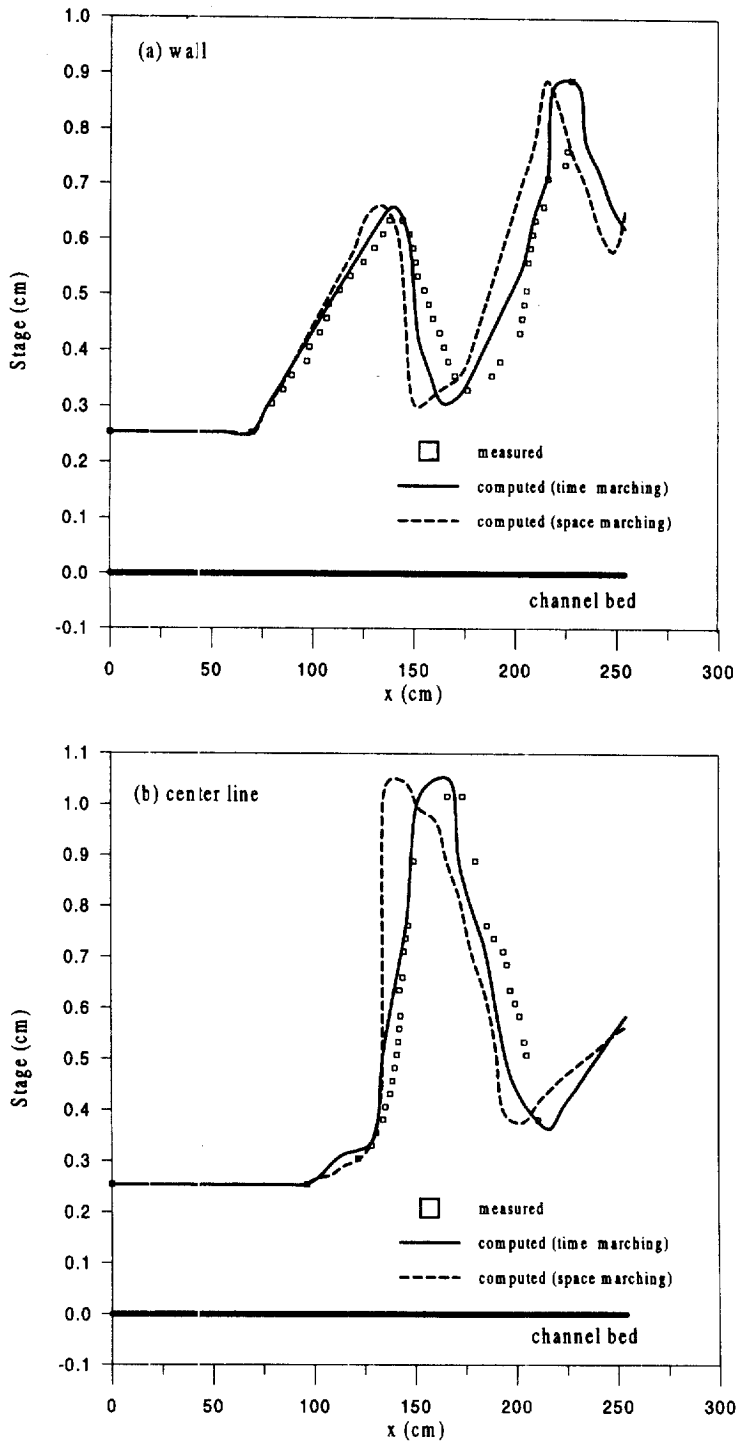
Fig. 7. Froude number and specific energy profiles along the center line for Ippen's circular-arc channel contraction.

ing scheme gives better results than the space-marching scheme, similar to what is observed in the preceding section. The time-marching scheme makes good prediction on the phase along the center line as well. There also exists a distinct phase difference between the experimental and computed results along the wall. Chaudhry and Bhallamudi [10] suggested that the errors in the computed results along the center line of the transition section are probably attributable to vio-
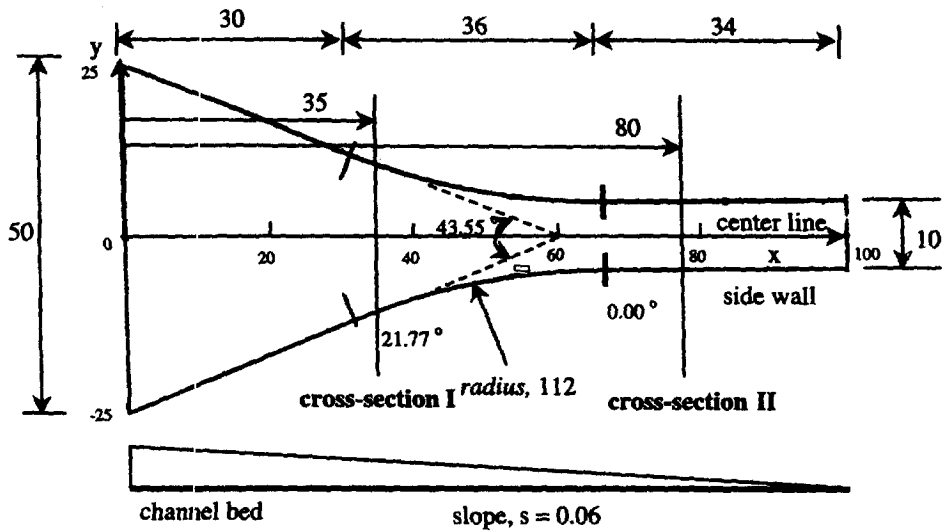
Fig. 8. Definition sketch of the channel contraction, the TPWCB channel.

lation of the hydrostatic pressure assumption at steep surface gradients and the effect of air entrainment. The transverse water-surface profiles at cross-sections I (x = 35 cm) and II (x = 80 cm) are plotted in Fig. 10(a) and (b), respectively. The computed water surfaces are symmetrical about the center line of the channel. The asymmetry of the experimental data is caused by a small slope variation of 0.001 in the channel cross sections of the existing experimental setup.

To further investigate the accuracy of two numerical approaches, the Froude number and specific energy obtained from the numerical simulations are compared with that from the experiments. As depicted in Fig. 11, the locations of maximum Froude number predicted by the numerical simulation are roughly the same as those by the experiment. However, the differences in values between the experiment and the two numerical simulations increase when $x \geqslant 60$ cm, and the simulation peak value at x = 86 cm is about 15% greater than experimental one. Figure 12 compares the specific energy profiles. It reveals discrepancies in the same area as the Froude number (Fig. 11), though the numerical simulation by the time-marching approach gives better agreement with the experiment than that by the space-marching. In other words, the two numerical models fail to very precisely predict the hydrodynamic effect as well as the specific energy, and thus have caused phase differences. According to Fig. 12, both the space- and time-marching approaches simulate well the specific energy when $x < 50$ cm. In the region where a shock wave forms ($x \geqslant 50$ cm), however, the time-marching approach simulates the specific energy better, though it needs 17 times more CPU time than the space-marching approach in this case.

A possible reason for the discrepancy may be the inaccuracy in estimation of the source/sink term in the governing equation in the numerical modeling or the neglect of the turbulence resistance. However, according to Molls and Chaudhry [7], the inclusion of turbulent viscosity in the simulation of the supercritical flow also results in a significant phase difference between simulation and measurement. As a result, phase difference could more probably come from the biased estimation of a source/sink term in the governing equation. Source/sink terms in Equation (1) include S_o and S_f, which represent the slope of the channel bed and that of friction, respectively. Since S_o is constrained by the geometric form of the experiment, S_f is the term with possible inaccuracy in estimation [19].

In this study, S_f is represented by Manning's formula using a constant roughness value throughout the simulation area. Chow [1] described the influence of Manning's n under different Froude numbers and flow depths. According to his experimental result, Wu [20] has shown that Manning's n increases with depth in supercritical flow. In order to model the oblique shock
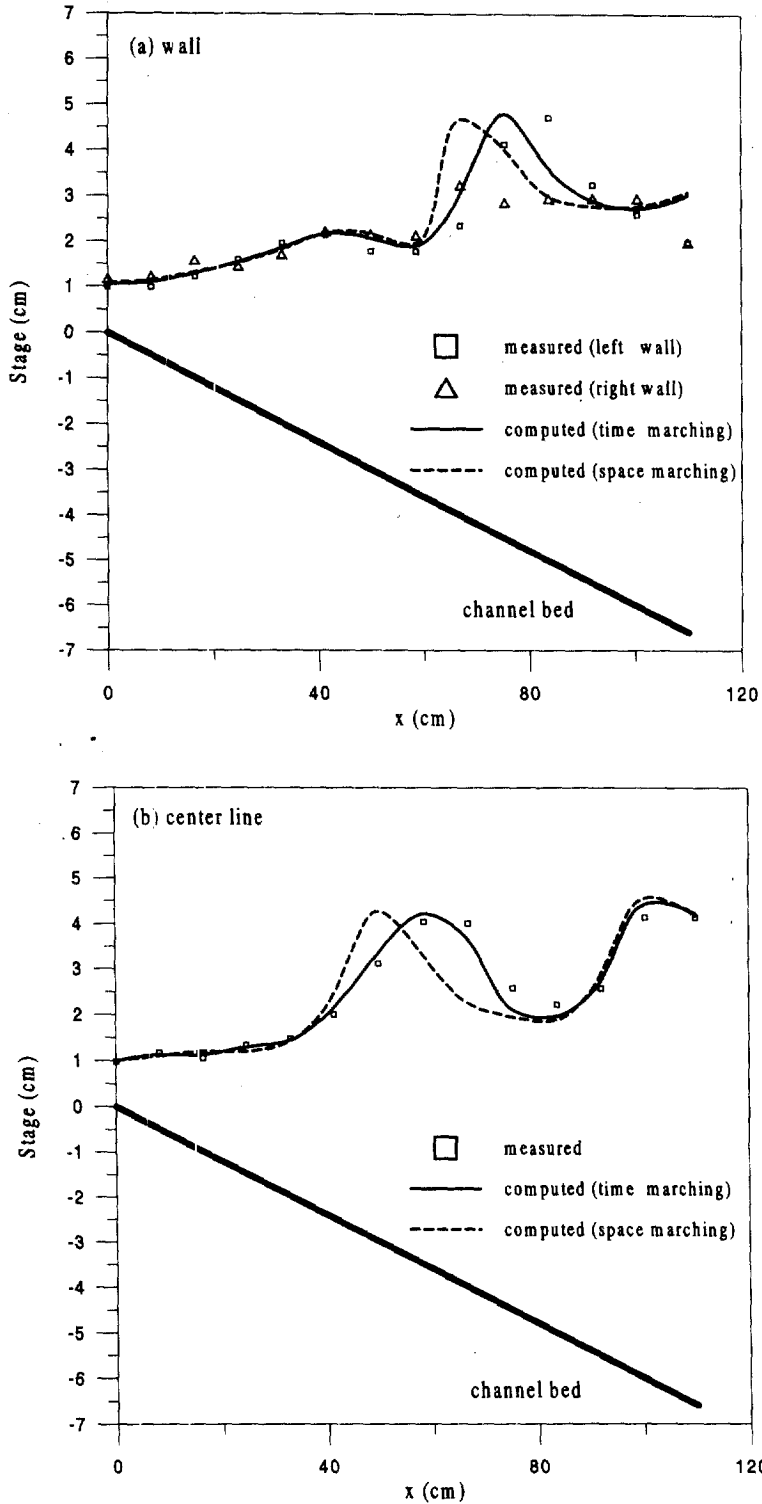
Fig. 9. Water surface profiles along the wall and the center line for the TPWCB channel.

wave precisely under any turbulent flow conditions. The S_f term described in the Manning or Chezy formula has to be carefully examined, for instance, establishing a functional relationship of water depth and the value of Manning n or Chezy C under different Froude numbers in supercritical flow.
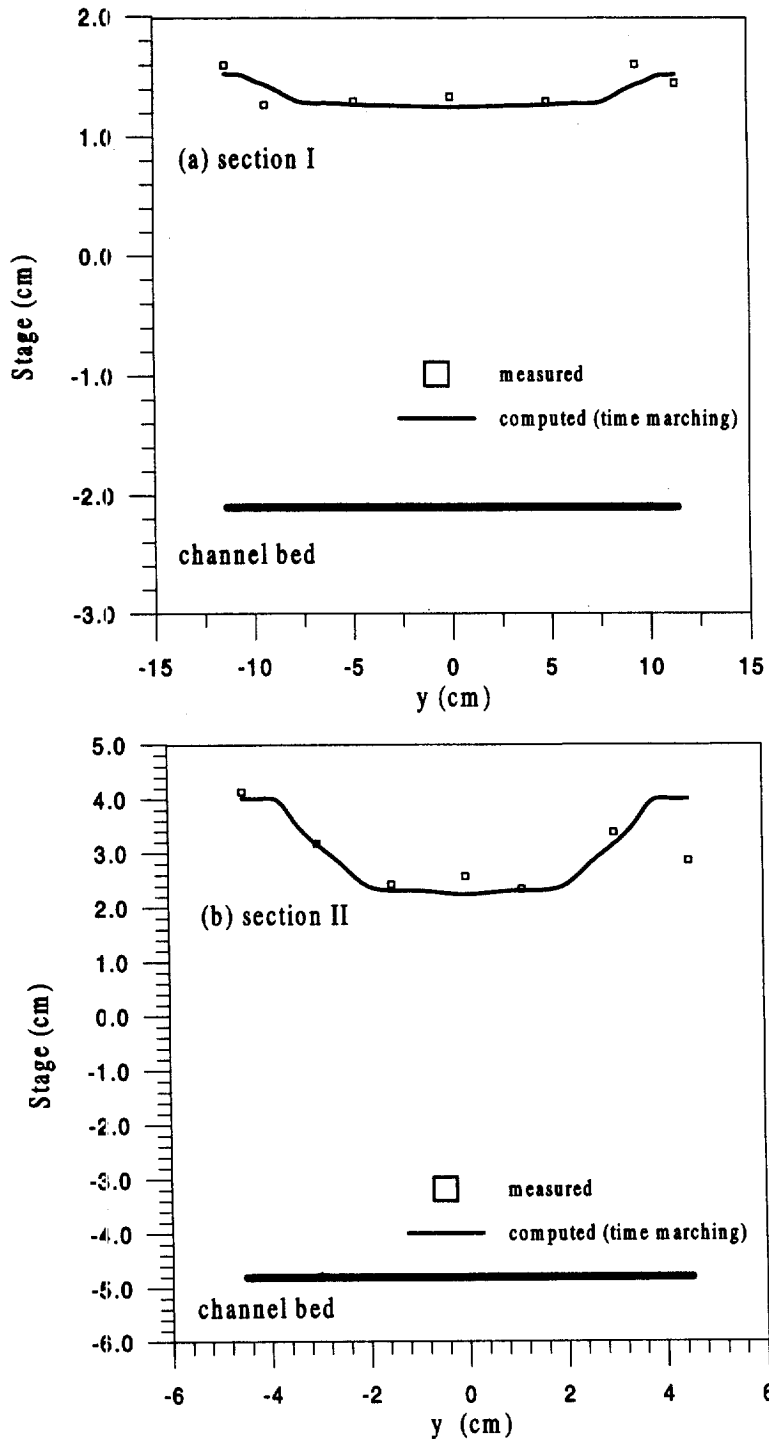
Fig. 10. Transverse water surface profiles at cross-sections I and II for the TPWCB channel.

7. CONCLUSIONS

This paper describes two numerical approaches, one marching in time and the other in space, by which to solve the two-dimensional shallow-water equations for supercritical flow in a channel contraction. Both approaches employ the high-resolution finite-difference scheme that is efficient for discontinuous regions such as shock waves and rapidly varied flow conditions. The
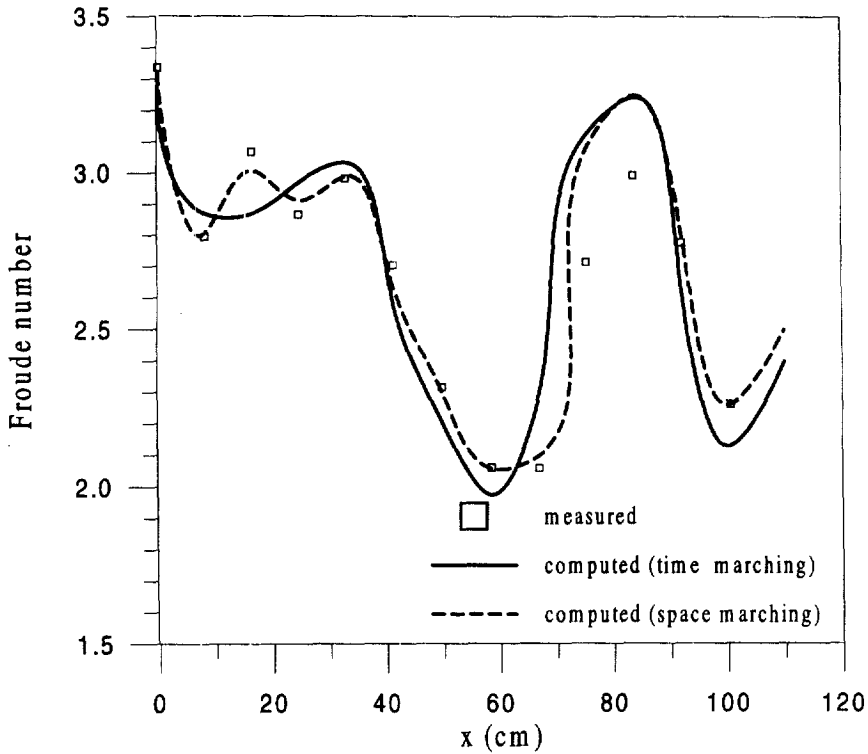
Fig. 11. Froude number profiles along the center line for the TPWCB channel.

computed results show that both approaches are generally in reasonable agreement with the measured data, and that the time-marching approach is more accurate than the space-marching one but consumes more CPU time. The phase difference between the computed and measured results in channel contraction is noticeable when the effect of non-hydrostatic pressure distri-
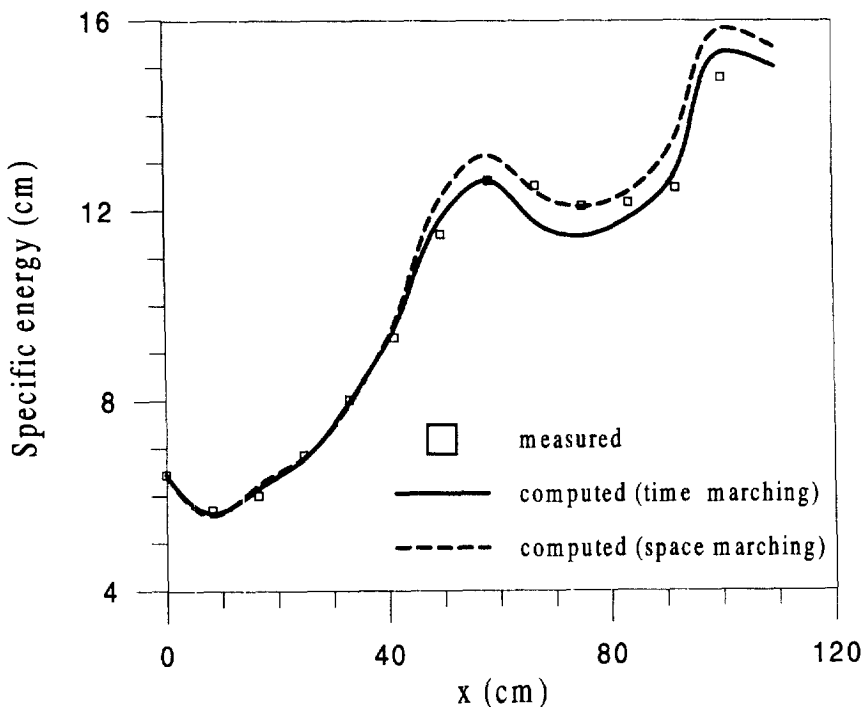

Fig. 12. Specific energy profiles along the center line for the TPWCB channel.

bution, air entrainment and the inaccuracy in estimation of source/sink terms in the governing equation are predominant. Nevertheless, the computed results can be used effectively for determining the design height of hydraulic structures.

REFERENCES

1. V. T. Chow, *Open-Channel Hydraulics*, McGraw-Hill New York, 1959.
2. Ippen, A. T., Mechanics of supercritical flow. *Transaction ASCE*, 1951, **116, 268–295**.
3. Garcia, R. and Kahawita, R. A., Numerical solution of the St. Venant equations with the MacCormack finite-difference scheme. *International Journal for Numerical Methods in Fluid*, 1986, **6, 259–274**.
4. J. A. Cunge, F. M. Holly and A. Verwey, *Practical Aspects of Computational River Hydraulics*, Pitman, London, 1980.
5. Fennema, R. J. and Chaudhry, M. H., Explicit numerical schemes for unsteady free surface flows with shock. *Water Resources Research*, 1986, **22**(13), 1923–1930.
6. Jimenez, O. F. and Chaudhry, M. H., Computation of supercritical free-surface flow. *Journal of Hydraulic Engineering, ASCE*, 1988, **114**(4), 377–395.
7. Molls, T. and Chaudhry, M. H., Depth-averaged open-channel flow model. *Journal of Hydraulic Engineering, ASCE*, 1995, **121**(6), .
8. J. Kuipers and C. B. Vreugdenhill Calculations of two-dimensional horizontal flow. Rep. S163. Part 1. Delft Hydraulics Lab, Delft, The Netherlands, 1973.
9. Lai, C., Multicomponent-flow analyses by multimode method of characteristics. *Journal of Hydraulic Engineering, ASCE*, 1994, **120**(3), 378–395.
10. Chaudhry, M. H. and Bhallamudi, S. M., Computation of flows in open channel transitions. *Journal of Hydraulic Research*, 1992, **30**, 77–93.
11. J. F. Thompson, *Numerical Grid Generation Foundations and Applications*, North-Holland, Amsterdam, 1982.
12. M. H. Hsu, Numerical simulations of supercritical shock wave in open channel (I), Technical Report No. 149, Hydraulic Research Laboratory, NTU (in Chinese) 1993.
13. J. L. Randall, *Numerical methods for Conservation Laws*. Birkhauser, Basel, 1990.
14. Godunov, S. K., A difference scheme for numerical computation of discontinuous solutions of equations of hydrodynamics. *Math. Sb.*, 1959, **47, 271–290**.
15. Roache, P. J., Computational Fluid Dynamics. Hermosa Publishers, Albuquerque, N.M.
16. R. W. MacCormack, The effect of viscosity in hypervelocity impact cratering. Amer. Institute Aeronautics and Astronamtics (AIAA), Journal Paper No. 69–354. Cincinnati, Ohio, 1969.
17. Sweby, P. K., High resolution schemes using flux limiters for hyperbolic conservation laws. *Siam Number. Anal.*, 1984, **21**(5), 995–1011.
18. Ippen, A. T. and Dawson, J. H., Design of channel contractions. *Transaction ASCE*, 1951, **116, 326–346**.
19. Schaffranek, R. W. and Lai, C., Friction-term response to boundary-condition type in flow models. *Journal of Hydraulic Engineering, ASCE*, 1996, **122**(2), 73–81.
20. F. C. Wu, *The effects of bed slope and flow depth on the roughness coefficient of simulated vegetation.*, Conference of Agricultural Engineering, Taipei, Taiwan, 1994.

8. APPENDIX

Equation (28) can also be written in the form [9] as follows

$$F_x + CF_y = S \tag{49}$$

The Jacobian matrixes of Equation (49) are defined as from Equation (4) by chain rule [9]

$$C = \frac{\partial G}{\partial F} = \frac{\frac{\partial G}{\partial U}}{\frac{\partial F}{\partial U}} = A^{-1}B \tag{50}$$

Hence

$$C = A^{-1}B = \begin{bmatrix} 0 & 1 & 0 \\ c^2 - u^2 & 2u & 0 \\ -uv & v & u \end{bmatrix}^{-1} \begin{bmatrix} 0 & 0 & 1 \\ -uv & v & u \\ c^2 - v^2 & 0 & 2v \end{bmatrix} \tag{51}$$

and

$$C = \begin{bmatrix} \frac{2u}{u^2 - u^2} & \frac{-1}{u^2 - c^2} & 0 \\ 1 & 0 & 0 \\ \frac{v(u^2 - c^2)}{u(u^2 - c^2)} & \frac{-v}{u^2 - c^2} & \frac{1}{u} \end{bmatrix} \begin{bmatrix} 0 & 0 & 1 \\ -uv & v & u \\ c^2 - v^2 & 0 & 2v \end{bmatrix} \tag{52}$$

Then

$$C = \begin{bmatrix} \frac{uv}{u^2-c^2} & \frac{-v}{u^2-c^2} & \frac{u}{u^2-c^2} \\ 0 & 0 & 1 \\ \frac{c^2(u^2+v^2-c^2)}{u(u^2-c^2)} & \frac{-v^2}{(u^2-c^2)} & \frac{v(2u^2-c^2)}{u(u^2-c^2)} \end{bmatrix}$$

(53)

The characteristic equation corresponding to Equation (53) is written as:

$$\det(C - \lambda I) = 0$$

(54)

where I is unit matrix. The eigenvalues $\Lambda = [\lambda, \lambda^+, \lambda^-]^T$ of Equation (28) are three roots of λ in Equation (54), i.e.

$$\Lambda = [\lambda, \lambda^+, \lambda^-]^T$$

$$= \left[\frac{v}{u}, \frac{uv + c^2\sqrt{\frac{u^2+v^2}{c^2}-1}}{u^2-c^2}, \frac{uv - c^2\sqrt{\frac{u^2+v^2}{c^2}-1}}{u^2-c^2} \right]^T$$

(55)